Acta Materialia 155 (2018) 418–432

Contents lists available at ScienceDirect

Acta Materialia

journal homepage: www.elsevier.com/locate/actamat

Full length article

Compact reconstruction of orientation distributions using generalized spherical harmonics to advance large-scale crystal plasticity modeling: Verification using cubic, hexagonal, and orthorhombic polycrystals

Adnan Eghtesad, Timothy J. Barrett, Marko Knezevic*

Department of Mechanical Engineering, University of New Hampshire, Durham, NH, 03824, USA

ARTICLE INFO

Article history:
Received 31 March 2018
Received in revised form
2 June 2018
Accepted 4 June 2018
Available online 19 June 2018

Keywords:
Orientation distribution function
Microstructures
Anisotropic material
Crystal plasticity
Numerical algorithms

ABSTRACT

Compaction of crystallographic texture data is highly desirable in crystal plasticity simulations because the computational time involved in such calculations scales linearly with the number of crystal orientations. In a recent publication, we have reported a rigorous procedure for reducing large datasets of crystal orientations for cubic-orthotropic and hexagonal-orthotropic polycrystalline metals using symmetrized generalized spherical harmonics (GSH) functions. The procedure relies on a quantitative description of crystallographic texture using an orientation distribution function (ODF) and its series representation using GSH. The core procedure consists of matching the spectral representation of a full-size ODF containing any number of crystal orientations with that of an ODF containing a compact set of orientations. In this paper, we generalize the procedure to any crystal structure with no restrictions to sample symmetry. These major extensions are accompanied by dealing with significantly more dimensions as well as imaginary terms. Two approaches for generating an initial set of orientations in the compact ODF are explored, one based on binning of a given fundamental zone in the Bunge-Euler orientation space and another that takes advantage of MTEX to maximize the compaction. The overall procedure has been successfully applied to compaction of large ODFs for cubic, hexagonal, and orthorhombic polycrystalline metals with orthotropic and no sample symmetry. It is quantitatively demonstrated that texture evolution, twin volume fraction evolution, stress-strain response, and geometrical changes of samples can be accurately simulated to large plastic strains with compact ODFs using crystal plasticity finite element models.

1. Introduction

Crystallographic texture in a polycrystal can be quantitatively described by an orientation distribution function (ODF) [1], which is the normalized probability density associated with the occurrence of a given crystal orientation in the polycrystal. The ODF is an important microstructural feature influencing the anisotropy of various material properties [1–5]. Modeling the anisotropy of plastic properties and the evolution of anisotropy with plastic strain requires consideration of the crystal structure and crystal orientation because of their role in the activation of dislocation glide and deformation twinning mechanisms of plastic deformation [6]. Thus, any material model aimed at predicting anisotropic material properties and texture evolution must consider the ODF.

Many polycrystal plasticity models have been developed over the past several decades to predict discrete ODF-property relationships and their evolution. These models range from upper bound Taylor-type models [6,7], lower bound Sachs model [8,9], mean-field formulations such as visco-plastic self-consistent (VPSC) [10–14] and elasto-plastic self consistent (EPSC) [15,16], to the full-field crystal plasticity finite element (CPFE) models [17–21] and Green's function based models with a convolution integral solved using fast Fourier transforms (FFTs) [22,23]. More recently VPSC and EPSC models have been coupled with implicit FE framework [24–26].

* Corresponding author. Department of Mechanical Engineering, University of New Hampshire, 33 Academic Way, Kingsbury Hall, W119, Durham, NH, 03824, USA.
E-mail address: marko.knezevic@unh.edu (M. Knezevic).

https://doi.org/10.1016/j.actamat.2018.06.017
1359-6454/

Kinematics and kinetics of crystallographic slip and twinning in these models are physically based, which in combination with capturing ODF evolution makes these models essential for understanding and predicting microstructural processes and associated microstructure-property relationships. As such, these models are highly desirable for performing accurate simulations of metal forming processes. Many simulation cases include simple compression, simple tension, impact tests, cup-drawing, sheet hydroforming, bending, and other forming operations have been performed and reported in the literature [24,27–38]. These works demonstrated the utility of polycrystal plasticity models within FE simulation tools to achieve accuracy of simulations. However, the works emphasized that performing metal forming process simulations with polycrystal plasticity is a huge computational challenge. For example, the time for a compression simulation up to a strain of 0.2 with about 1000 elements and an ODF containing 1000 crystal orientations at each FE integration point was approximately 60 h on a regular PC [24]. Clearly, speedups are critically needed to make complex metal forming simulations with polycrystal plasticity constructive laws practical.

Recently, several computationally efficient numerical implementations of polycrystal plasticity have been developed. Common to these developments were databases of precomputed solutions to crystal plasticity equations in order to circumvent solving sets of very stiff equations requiring many iterations for every crystal at every trial time increment. One approach relies on adaptive sampling algorithms to build a database that constantly updates itself during calculations [39,40]. The method improved the computational speed involved by about an order of magnitude. Some other database approaches store precompiled solutions in the form of spectral coefficients of continuous GSH basis [41–45] or FFTs [46–49]. These implementations resulted with significant reductions in computational time approaching two orders of magnitude. A process plane concept, based on proper orthogonal decomposition in Rodrigues orientation space, has been conceived to yield some improvements as well [50]. Additionally, several high performance computational application for crystal plasticity have been developed to run on graphic processing unit (GPU) hardware [51–54]. All of these studies have focused on the crystal plasticity solvers. While successful in accelerating the calculations, none of the above approaches attempted to minimize the amount of state variable data related to the ODF. Since polycrystal plasticity calculations scale linearly with the number of crystal orientations involved in calculations, the computational speed can further be reduced by the development of an ODF data compaction procedure.

Several studies for approximating a given ODF with the minimum number of crystal orientations representing the ODF have been carried out in the past [55–58]. The most successful method relied on a suitably defined error difference between a measured ODF and a representative ODF containing discrete crystal orientations [56,58]. The number of discrete orientations was systematically increased until the error was minimized. The estimated number of orientations varied with respect to the measured ODF. Part of the reason for this variation is because weights of individual orientations were not adjusted. More conveniently, an ODF can be represented by a weighted set of discrete orientations if these orientations are appropriately chosen. To this end, the fundamental problem is determining the minimal set of these discrete orientations.

In a recent paper [59], we have presented a rigorous procedure for reducing large datasets of crystal orientations using GSH functions. The procedure involves matching the expansion coefficients of a full-size ODF containing any number of crystal orientations with those of an ODF containing a compact set of orientations. The procedure was applied to metals with cubic and hexagonal crystal structure restricted to orthotropic sample symmetry. This paper generalizes the procedure to any crystal structure with no restrictions to sample symmetry. In particular, the symmetrized GSH for orthorhombic crystal symmetry is used. As a result, any given ODF can be compacted to a computationally manageable ODF, which is at the same time representative and matches qualitatively and quantitatively the starting ODF. These major extensions are accompanied by dealing with significantly more dimensions as well as imaginary terms. Moreover, we explore two approaches for generating an initial set of orientations in the compact ODF, one based on binning of a given fundamental zone in the Bunge-Euler orientation space and another that takes advantage of MTEX to maximize the compaction. Taking advantage of the linearity of the Fourier space, a linear programming problem is then set to match the expansion coefficients of the given ODF with those of a compact ODF by varying the weights of orientation in the compact ODF. Finally, a minimum number of weighted orientations in the compact ODF is determined and used in modeling of ODF-property relationships and their evolution. The development of the procedure along with several case studies verifying the procedure will be described in this paper. In particular, quantitative agreement between crystal plasticity calculations of texture evolution, twin volume fraction evolution, stress-strain response, and geometrical changes of samples using measured ODFs and compact ODFs will be demonstrated for several polycrystalline metals with cubic, hexagonal, and orthorhombic crystal structures.

2. Spectral representation of ODF using GSH

ODF, which will be denoted by $f(g)$, represents the normalized probability density that quantifies the occurrence of the crystallographic orientation, g, in the sample and is expressed as:

$$f(g)dg = \frac{dV}{V}, \quad \int_{FZ} f(g)dg = 1, \tag{1}$$

where V is the physical volume of a material and dV is the volume of material associated with a lattice orientation dg. The FZ stands for a fundamental zone, which is an asymmetrical domain of all physically distinct orientations of the local crystal that can occur in the material [1,60]. Size of FZ depends on crystal and sample symmetry which will be describe later. Crystal lattice orientation is described by three independent variables through either a matrix of direction cosines, a set of Bunge-Euler angles [1], an angle-axis couple [61], a Rodriguez vector [62], or a set of quaternions [63]. Here we use the Bunge-Euler space and three Bunge-Euler angles to describe every crystal orientation belonging to an ODF. Every crystal orientation is thus an ordered set of three rotation angles $g = (\varphi_1, \Phi, \varphi_2)$ that collectively transform the crystal local frame to the sample reference frame.

The ODF can be developed in a series of GSH as follows [1,64]:

$$f(g) = \sum_{l=0}^{\infty} \sum_{m=-l}^{+l} \sum_{n=-l}^{+l} F_l^{mn} T_l^{mn}(g), \tag{2}$$

where, T_l^{mn} and F_l^{mn} are the GSH function and complex coefficients representing the ODF, respectively. The value of l determines the total number of dimensions involved in the GSH series. The capital letter L will be used to indicate the upper limit for the l values.

In terms of Bunge-Euler angles, the representation from Eq. (2) is

$$f(\varphi_1, \Phi, \varphi_2) = \sum_{l=0}^{\infty} \sum_{m=-l}^{+l} \sum_{n=-l}^{+l} F_l^{mn} e^{im\varphi_2} P_l^{mn}(\cos\Phi) e^{in\varphi_1}, \tag{3}$$

where, $P_l^{mn}(\cos\Phi)$ are Legendre functions [1]. To economically represent an ODF using GSH, crystal and sample (statistical) symmetries are embedded into GSH [1]. For example, Eq. (2) for cubic-orthotropic[1] can be written as follows

$$f(g) = \sum_{l=0}^{\infty} \sum_{\mu=1}^{M(l)} \sum_{\nu=1}^{N(l)} F_l^{\mu\nu} \dddot{T}_l^{\mu\nu}(g), \tag{4}$$

where, the dots on top of the GSH function denote the crystal and sample symmetries. The limits to linearly independent indices, *M(l)* and *N(l)*, depend on selected crystal and sample symmetry [1]. These limits determine the number of dimensions used for the representation of a given ODF in an infinite dimensional space. The adopted notation for the symmetrized GSH functions is $\dddot{T}_l^{\mu n}$ for cubic-triclinic, $\dddot{T}_l^{\mu\nu}$ for cubic-orthotropic, $\ddot{T}_l^{\mu n}$ for hexagonal-triclinic, $\ddot{T}_l^{\mu\nu}$ for hexagonal-orthotropic, $\dot{T}_l^{\mu n}$ for orthorhombic-triclinic, and $\ddot{T}_l^{\mu\nu}$ for orthorhombic-orthotropic crystals. Note that triclinic means no sample symmetry so no dots are placed on top of the functions, while a single dot is placed to denote orthotropic symmetry, which is typical for an ODF in a rolled sheet.

As an example, a GSH function with combined crystal and sample symmetry for the representation in Eq. (4) is calculated using

$$\dddot{T}_l^{\mu\nu}(g) = \sum_{m=-l}^{+l} \sum_{n=-l}^{+l} \dddot{A}_l^{m\mu} \dot{A}_l^{n\nu} T_l^{mn}(g), \tag{5}$$

where, $\dddot{A}_l^{m\mu}$ and $\dot{A}_l^{n\nu}$ are symmetry coefficients fulfilling the crystal and sample symmetries, respectively [1].

In order to evaluate the expansion coefficients $F_l^{\mu\nu}$ in Eq. (4), the orthogonality relation for the GSH functions $\dddot{T}_l^{\mu\nu}$ is used

$$\int_{FZ} \dddot{T}_l^{\mu\nu}(g) \dddot{T}_{l'}^{*\mu'\nu'}(g) dg = \frac{1}{2l+1} \delta_{ll'} \delta_{\mu\mu'} \delta_{\nu\nu'}. \tag{6}$$

The asterisk symbol (*) in the superscript denotes the complex conjugate. The invariant orientation element *dg* in Bunge-Euler space is defined as

$$dg = \sin(\Phi)\ d\varphi_1\ d\Phi\ d\varphi_2. \tag{7}$$

To take the advantage of Eq. (6), both sides of Eq. (4) with prime indices are multiplied by the complex conjugate $\dddot{T}_l^{*\mu\nu}$ to get

$$\int_{FZ} f(g) \dddot{T}_l^{*\mu\nu}(g) dg = \sum_{l'=0}^{\infty} \sum_{\mu'=1}^{M(l')} \sum_{\nu'=1}^{N(l')} F_{l'}^{\mu'\nu'} \int_{FZ} \dddot{T}_{l'}^{\mu'\nu'}(g) \dddot{T}_l^{*\mu\nu}(g) dg. \tag{8}$$

The expansion coefficients are

$$F_l^{\mu\nu} = (2l+1) \int_{FZ} f(g) \dddot{T}_l^{*\mu\nu}(g) dg. \tag{9}$$

[1] The first symmetry refers to symmetry at the crystal level, while the second symmetry refers to statistical symmetry at the sample level.

The procedure for the compact reconstruction of ODFs advanced in this paper is based on the GSH representation of the ODFs. Expansion coefficients of any given ODF containing any number of crystal orientations are evaluated to represent a point in an infinite-dimensional space. We will refer to this point as the target point. These expansion coefficients can be matched with those of another equivalent ODF by solving a linear programing problem in the space of expansion coefficients. This recognition is in the core of the procedure for obtaining compact ODFs, which is described next.

3. Procedure for compact reconstruction of ODFs

The procedure for compacting a given ODF containing a large number of weighted crystal orientation, which will be referred to as the target ODF, produces an equivalent ODF containing a much smaller number of weighted crystal orientations, which will be referred to as the compact ODF. The GSH automated procedure is developed and fully automated in MATLAB [65]. Fig. 1 shows a flowchart describing the main steps involved in the procedure. Expansion coefficients of a target ODF are calculated using Eq. (9) to set the target point in the multidimensional space with orthogonal axis defined by the value of the expansion coefficients. Next, we create compact ODFs. To this end, we explore two approaches, one based on binning of a given fundamental zone in Bunge-Euler orientation space and another that takes the advantage of MTEX to maximize the compaction. Weights of crystal orientations in the compact ODF are adjusted during the solution procedure. Note that the number and positions of orientations are not adjusted during the solution procedure. The supplementary material of the paper contains the code.

3.1. Fundamental zones of crystal orientations

The set of all distinct crystal orientations that can occur in the sample is the fundamental zone (*FZ*). After consideration of crystal and sample symmetries, redundancies in orientation occurrences within Bunge-Euler space $\{ g = (\varphi_1, \Phi, \varphi_2) \mid, \ 0 \le \varphi_1 < 2\pi, \ 0 \le \Phi \le \pi, \ 0 \le \varphi_2 < 2\pi \}$ can be eliminated to derive a sub-space, the smallest of which is the *FZ* containing the physically distinct and non-redundant orientations. The size of *FZ* depends on crystal and sample symmetry. Fundamental zones within Bunge-Euler orientation space corresponding to relevant crystal-sample symmetries used in present work are presented in Table 1. Their geometrical representation is shown in Fig. 2. The geometrical representation of a *FZ* is not unique. Note that two *FZs* are presented for the cubic-triclinic case, one conveniently termed as a 'loaf' and another termed as a 'roof', based on their shapes. The loaf *FZ* is widely used in the literature [66]. However, we point out that it is not convenient to reduce the loaf *FZ* to the cubic-orthotropic *FZ*. It is convenient to derive an orthotropic *FZ* by performing three rotations of the type $\frac{\pi}{2}\langle 100\rangle$. As a result, $0 \le \varphi_1 < 2\pi$ reduces to $0 \le \varphi_1 < \frac{\pi}{2}$. This is possible with the roof *FZ*, which is used in the present paper. The *FZs* are used to define sets of crystal orientations covering respected orientation spaces. These sets will be termed master sets as described next.

3.2. Master set ODFs

In order to form master sets of crystal orientations, the fundamental zones are appropriately discretized into equal volume bins. The binning procedure has been described in previous works [59,66]. Each bin has six corner orientations and one orientation at the center. While the centers yield a more uniform texture, the corners ensure the complete coverage of the orientation space with a bigger data set. The bins are created by enforcing the invariant

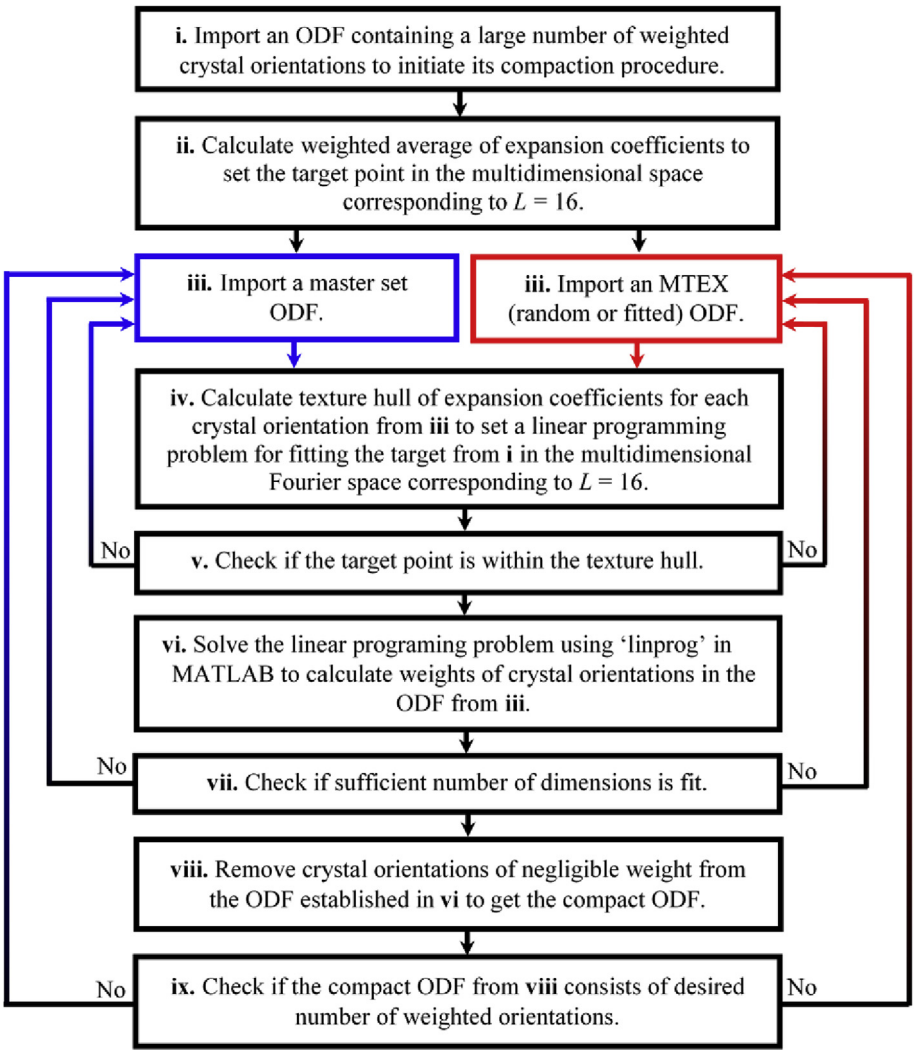

Fig. 1. Flowchart showing steps involved in the automated procedure for reducing a given ODF into an equivalent but compact ODF. While the master set ODF must increase the number of weighted orientation to achieve the desired accuracy, the MTEX ODF can cycle with either a constant number of weighted orientation due to the randomness of the selection in MTEX or an increased number of weighted orientations to achieve the desired accuracy.

volume integrals of

$$dV = \int dg = \int_{\Delta\varphi_2} \int_{\Delta\Phi} \int_{\Delta\varphi_1} \sin(\Phi) d\Phi d\varphi_1 d\varphi_2. \quad (10)$$

Selected values for the invariant volume defines number of orientations per master set. Table 2 summarizes the mesh of bins for each of the *FZs* and therefore defines the possible master sets of orientations. Note that either corner or center orientations can be considered. The resulting master set ODFs are conveniently uniform because they result from invariant volume bins.

3.3. MTEX (uniform or fitted) ODFs

Another scheme to define a starting set of orientations for the ODF compaction procedure is based on MTEX [67]. To this end, we either output a uniform ODF or a fitted ODF from MTEX. The latter is pre-fitted towards the target ODF using MTEX. Generation of either a statistically uniform ODF or a fitted ODF using built-in functions in MTEX will not be elaborated in more details because MTEX manual describes it and the reader is referred to the manual. Note that here, the number of orientations per MTEX compact ODF can vary and is not fixed like in Table 2 for master set ODFs. This contributes to the flexibility of the procedure involving MTEX. Moreover, the MTEX methods always produces a different ODF (even for the same number of orientations) to varying degrees of accuracy (i.e. some ODFs are better guesses than others). This is the premise of the iteration over MTEX fitted/MTEX uniform.

3.4. Finding compact ODFs by solving a linear programing problem

Expansion coefficients corresponding to individual crystal orientations within the mater set ODFs or those within MTEX (uniform or fitted) ODFs represent convex regions. These convex regions are referred to as the texture hulls in the multidimensional space [9,44,68,69]. These works presented orthotropic convex hulls for the cubic and hexagonal crystal structures. In order to solve the linear programing problem, a target point corresponding to the coefficients of a target ODF in the multidimensional space must be contained within the hull. The procedure ensures that the target point is within the texture hull. If not, another ODF is imported, as the backward arrows show in Fig. 1.

As mentioned above, texture hulls are composed of points the multidimensional space, where the number of dimensions depends

Table 1
Fundamental zones within Bunge-Euler orientation space as a function of crystal and sample symmetries.

Fundamental zone	Crystal symmetry	Sample symmetry
$FZ_{\text{Loaf}} = \left\{ \begin{array}{l} (\varphi_1, \Phi, \varphi_2) \vert 0 \le \varphi_1 < 2\pi, \\ \cos^{-1}\left(\frac{\cos\varphi_2}{\sqrt{1+\cos^2\varphi_2}}\right) \le \Phi \le \frac{\pi}{2}, \\ 0 \le \varphi_2 \le \frac{\pi}{4} \end{array} \right\}$	Cubic	Triclinic
or $FZ_{\text{Roof}} = \left\{ \begin{array}{l} (\varphi_1, \Phi, \varphi_2) \vert 0 \le \varphi_1 < 2\pi, \\ \cos^{-1}\left(\frac{\sin\varphi_2}{\sqrt{1+\sin^2\varphi_2}}\right) \le \Phi \le \frac{\pi}{2}, 0 \le \varphi_2 \le \frac{\pi}{4} \\ \cos^{-1}\left(\frac{\cos\varphi_2}{\sqrt{1+\cos^2\varphi_2}}\right) \le \Phi \le \frac{\pi}{2}, \frac{\pi}{4} \le \varphi_2 \le \frac{\pi}{2} \end{array} \right\}$		
$FZ = \left\{ \begin{array}{l} (\varphi_1, \Phi, \varphi_2) \vert 0 \le \varphi_1 < \frac{\pi}{2}, \\ \cos^{-1}\left(\frac{\sin\varphi_2}{\sqrt{1+\sin^2\varphi_2}}\right) \le \Phi \le \frac{\pi}{2}, 0 \le \varphi_2 \le \frac{\pi}{4} \\ \cos^{-1}\left(\frac{\cos\varphi_2}{\sqrt{1+\cos^2\varphi_2}}\right) \le \Phi \le \frac{\pi}{2}, \frac{\pi}{4} \le \varphi_2 \le \frac{\pi}{2} \end{array} \right\}$	Cubic	Orthotropic
$FZ = \left\{ \begin{array}{l} (\varphi_1, \Phi, \varphi_2) \vert 0 \le \varphi_1 < 2\pi, \\ 0 \le \Phi \le \frac{\pi}{2}, \\ 0 \le \varphi_2 \le \frac{\pi}{3} \end{array} \right\}$	Hexagonal	Triclinic
$FZ = \left\{ \begin{array}{l} (\varphi_1, \Phi, \varphi_2) \vert 0 \le \varphi_1 < \frac{\pi}{2}, \\ 0 \le \Phi \le \frac{\pi}{2}, \\ 0 \le \varphi_2 \le \frac{\pi}{3} \end{array} \right\}$	Hexagonal	Orthotropic
$FZ = \left\{ \begin{array}{l} (\varphi_1, \Phi, \varphi_2) \vert 0 \le \varphi_1 < 2\pi, \\ 0 \le \Phi \le \frac{\pi}{2}, \\ 0 \le \varphi_2 \le \pi \end{array} \right\}$	Orthorhombic	Triclinic
$FZ = \left\{ \begin{array}{l} (\varphi_1, \Phi, \varphi_2) \vert 0 \le \varphi_1 < \frac{\pi}{2}, \\ 0 \le \Phi \le \frac{\pi}{2}, \\ 0 \le \varphi_2 \le \pi \end{array} \right\}$	Orthorhombic	Orthotropic

on L. Table 3 summarizes the number of dimensions for given L values. Note that the number of dimensions scales inversely with the level of symmetry. It has been shown that the coefficients beyond $L = 16$ are insignificant for an ODF representation [59]. EDAX orientation imaging microscopy (OIM) analysis software, TexSEM Laboratories (TSL), uses the default value for L as $L = 16$ [70]. The representation of ODF-elastic stiffness relationship requires only $L = 4$, while the representation of ODF-yield stress requires L to about 10 or 12 [9,42,71]. Therefore, the present study will not consider coefficients beyond $L = 16$.

As mentioned above, Eq. (9) allows visualization of ODF as a point with the coordinates of $\overline{F}_l^{\mu\nu}$. We place the bar on top of these coefficients representing an ODF to indicate an averaged value of the coefficients based on the weights of crystal orientations in the ODF. Similarly, the coefficients of a single crystal, k, can be evaluated and also visualized as a point. The single crystal coefficients, ${}^kF_l^{\mu\nu}$, are used to define the hull of points. The space in between the points can be populated as a linear combination of the points so the hull is guaranteed to be compact and convex. As a result, the texture hull represents the complete set of all physically realizable ODFs [72]. Thus, the texture hull containing a given average ODF can be formally defined as

$$M = \left\{ \overline{F}_l^{\mu\nu} \;\middle|\; \overline{F}_l^{\mu\nu} = \sum_k {}^k\alpha \, {}^kF_l^{\mu\nu},\ {}^kF_l^{\mu\nu} \in M^k,\ {}^k\alpha \ge 0,\ \sum_k {}^k\alpha = 1 \right\}$$
$$M^k = \left\{ {}^kF_l^{\mu\nu} \;\middle|\; {}^kF_l^{\mu\nu} = (2l+1)\, T^{*\mu\nu}_l\left(g^k\right),\ g^k \in FZ \right\} \tag{11}$$

Fig. 3 illustrates the real and imaginary texture hulls for cubic, hexagonal, and orthorhombic crystal structures with triclinic sample symmetry. The first three coefficients are plotted in every case. We emphasize that any physically realizable ODF has to have a representation inside the corresponding hull. Fig. 3 also depicts a few points corresponding to the measured textures, which will be used to demonstrate the utility of the developed procedure. These textures will be used as the full-size target ODFs for which equivalent compact ODFs will be sought.

The linear programming problem consists of finding an appropriate weight of expansion coefficients for each orientation in the respected compact ODF to match expansion coefficients of the target ODF. The solver starts with equal weight orientations within the compact ODF. In the cases of master set ODFs and MTEX uniform ODFs, the initial ODFs are uniform and the corresponding

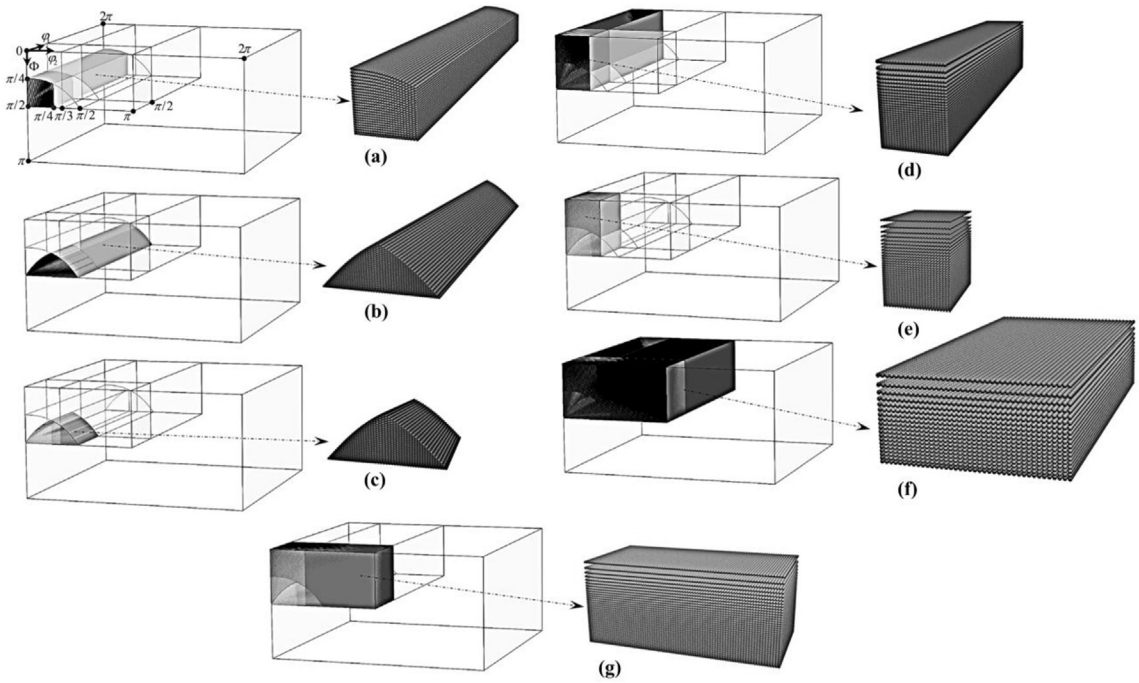

Fig. 2. Fundamental zones within Bunge-Euler orientation space corresponding to crystal-sample symmetries as presented in Table 1 i.e.: (a) 'loaf' cubic-triclinic, (b) 'roof' cubic-triclinic, (c) cubic-orthotropic, (d) hexagonal-triclinic, (e) hexagonal-orthotropic, (f) orthorhombic-triclinic, and (g) orthorhombic-orthotropic.

Table 2
Number of orientations in mater set ODFs for given symmetries and dV.

Crystal-sample symmetry	dV [$^\circ{}^3$]	# of bin centers	# of bin corners	dV [$^\circ{}^3$]	# of bin centers	# of bin corners
Cubic-triclinic (roof)	2.26	2700	3960	3.81	1472	2350
Cubic-orthotropic (roof)	0.53	3240	4200	1.03	1568	2176
Hexagonal-triclinic	5.97	3290	4224	15.43	1225	1728
Hexagonal-orthotropic	1.70	2992	3672	6.37	770	1056
Orthorhombic-triclinic	13.61	4165	5184	19.91	2790	3584
Orthorhombic-orthotropic	5.82	2530	3168	14.89	952	1296

Table 3
Numbers of dimensions from non-zero frequencies for selected L values. Note that the first frequency is always ($Re = 1$, $Im = 0$) and is not counted. Note also that, in addition to longer series expansion, triclinic ODFs have real and imaginary terms, which were counted separately.

	$L = 4$	$L = 6$	$L = 8$	$L = 10$	$L = 12$	$L = 14$	$L = 16$
Cubic-triclinic	18	44	78	158	258	370	564
Cubic-orthotropic	3	7	12	22	36	50	75
Hexagonal-triclinic	28	80	178	300	496	778	1100
Hexagonal-orthotropic	5	13	26	42	68	104	145
Orthorhombic-triclinic	88	236	496	900	1480	2268	3296
Orthorhombic-orthotropic	14	34	68	120	194	294	424

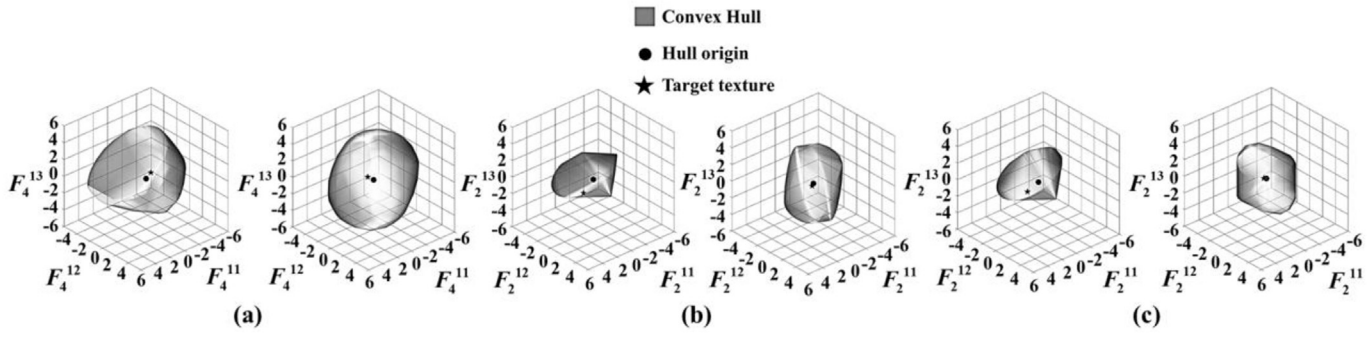

Fig. 3. Texture hulls in the first three dimensions for: (a) cubic-triclinic, (b) hexagonal-triclinic, and (c) orthorhombic-triclinic materials. Target ODFs for Cu in (a), Ti in (b), and SW U along with origins are indicated in the respected hulls.

Table 4
Experimentally measured texture data used in case studies as target ODFs.

Material	Crystal structure	Sample symmetry	Technique	# of weighted orientations
Pure Cu	Cubic (FCC)	Triclinic	Numerical	50,000
AA6022-T4	Cubic (FCC)	Orthotropic	EBSD	119,248
Pure Ta	Cubic (BCC)	Orthotropic	XRD	184,464
Pure α-Zr	Hexagonal	Triclinic	XRD	100,000
WE43	Hexagonal	Triclinic	EBSD	100,000
High purity α-Ti	Hexagonal	Triclinic	Neutron	50,000
Depleted α-U (SR)	Orthorhombic	Triclinic	EBSD	80,434
Depleted α-U (SW)	Orthorhombic	Triclinic	EBSD	128,780
Depleted α-U (CR)	Orthorhombic	Orthotropic	EBSD	295,600

expansion coefficients are approximately at the origin of the respected hulls. Any deviation from the equally weighted orientations makes these ODFs non-uniform, shifting their expansion coefficients from the origin. The weighted average of the expansion coefficients corresponding to the compact ODF is evolving during fitting until it is equal to that of the target ODF. The solution is available as long as the target point is within the hull of the compact ODF. The number of dimensions used in the fitting procedure, defined by *L*, influences the accuracy of the representation as well the computational time involved in the procedure. The more dimensions used imply more accurate representations and longer computational times.

The equation and constraints to find a compact ODF matching an initial full size ODF are:

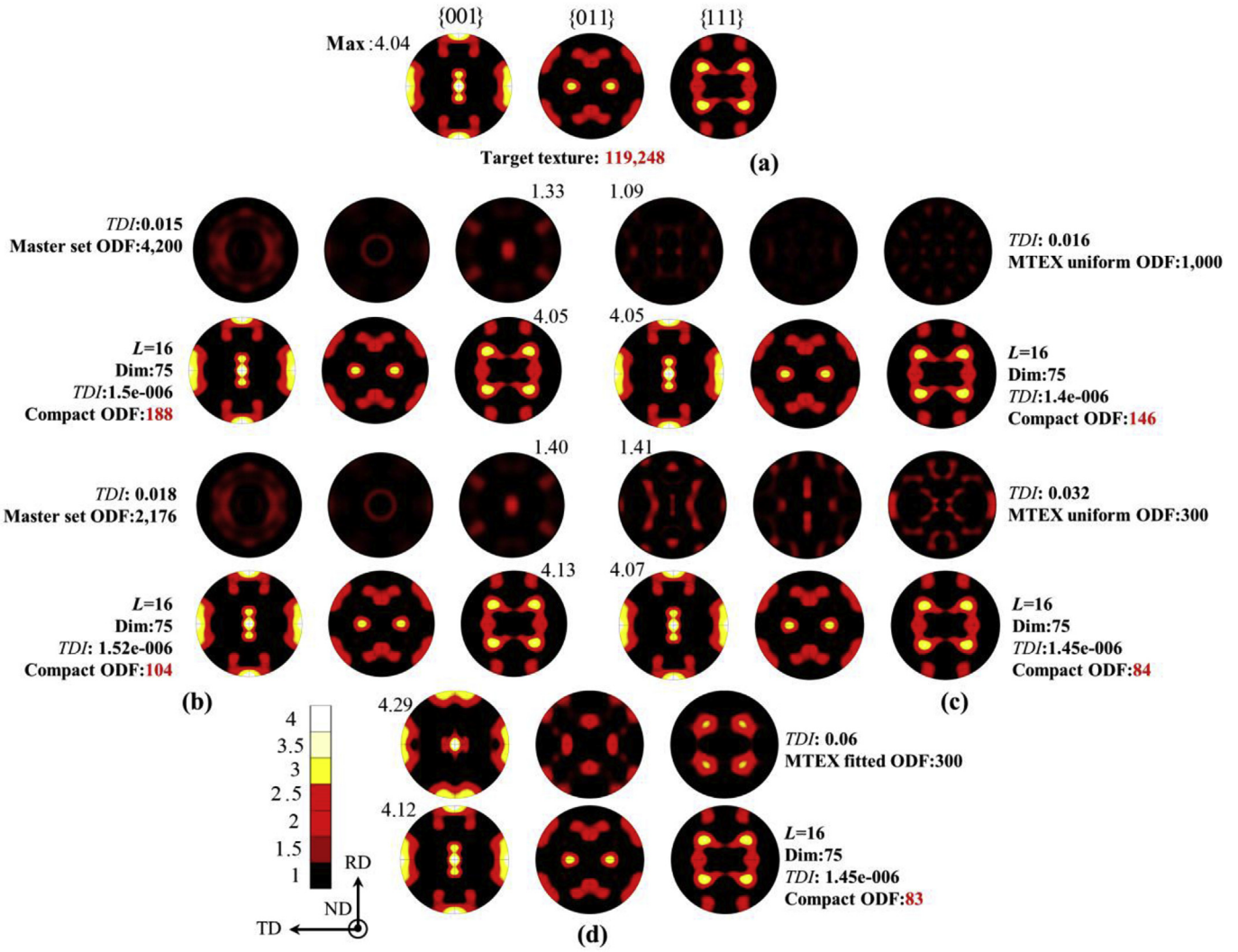

Fig. 4. Stereographic pole figures showing: (a) FCC-orthotropic target ODF of AA6022-T4, (b) initial master set ODF and final compact ODF, (c) initial MTEX uniform ODF and final compact ODF, (d) initial MTEX fitted ODF and final compact ODF. Note that two initial sets of crystal orientations were used in (b) and (c). *TDI* quantifies the difference between perfectly uniform texture and initial master set ODF, perfectly uniform texture and initial MTEX uniform ODF, target ODF and MTEX fitted ODF, and target ODF and compact ODF. Maximum intensity is indicated for each pole plot. *L* and Dim. indicates the number of dimensions fit in the space. Number of weighted orientations per ODF is indicated. In case *L* is not specified then pole figures are plotted with default $L = 16$.

$$\widehat{F}_l^{\mu\nu} = {}^k\alpha\, {}^kF_l^{\mu\nu},\ \sum_k^{N_{crys}} {}^k\alpha = 1,\ 0 \le {}^k\alpha \le 1, \tag{12}$$

Where, ${}^kF_l^{\mu\nu}$ are the expansion coefficients of individual orientations in the compact ODF and ${}^k\alpha$ are the unknown weights. We employ a linear programming solver "linprog" in MATLAB [73] to solve for the weights. The system of equations is set as

$${}^k\alpha\, {}^kF_l^{\mu\nu} - \overline{F}_l^{\mu\nu} - P_l^{\mu\nu} - Q_l^{\mu\nu} = 0,\ \sum_k^{N_{crys}} {}^k\alpha = 1, \tag{13}$$

inequality constraints are

$${}^k\alpha \ge 0,\ {}^k\alpha \le 1,\ P_l^{\mu\nu} \ge 0,\ Q_l^{\mu\nu} \ge 0, \tag{14}$$

and the objective function for minimization is

$$\sum_l \sum_\mu \sum_\nu \left(P_l^{\mu\nu} + Q_l^{\mu\nu}\right). \tag{15}$$

In this formulation, $P_l^{\mu\nu}$ and $Q_l^{\mu\nu}$ are slack variables. Number of slack variables depend on the number of available inequalities. Since two inequalities exist, two slack variables are needed for the linprog solver. The slack variables ensure equality constraint of the linear system of equations to be solved. The slack variables are positive and bounded in magnitude. The mathematical operations of summation and subtraction facilitate a wide variety of paths to obtain the solution. The fitting program stops upon reaching a prescribed tolerance defined by

$$\sqrt{\sum_l \sum_\mu \sum_\nu \left(\overline{F}_l^{\mu\nu} - \widehat{F}_l^{\mu\nu}\right)^2}. \tag{16}$$

The tolerance value is set to $TOL \le 10^{-12}$. It is necessary to ensure that the procedure fit as many dimensions as possible. In case the procedure fails to fit the desired number of dimensions, it cycles and another ODF is imported as shown by the backward arrows in Fig. 1. If based on the MTEX selection, the new ODF can contain the same number of different crystal orientations. Alternatively, the new ODF can have an increased number of crystal orientations generated either based on the MTEX selection or the *FZ* binning. The latter is used if the former fails to converge upon three trials. The number of discrete orientations in the new ODF is systematically increased until the procedure fits $L = 16$. However, $L = 16$ for low symmetry orthotropic structures can becomes excessive for the linprog MATLAB function and memory requirement.

Finally, the orientations with negligible weights are removed. In order to make sure that no appreciable error is introduced by removing these orientations, it is ensured that the summation of weights after the removal is greater than 0.99.

In closing this section, we introduce a convenient measure in order to quantify the quality of fits. The measure is termed texture difference index (*TDI*) [59,74]. The measure is used to quantify the accuracy of the spectral representation as a function of the dimensions in the infinite space because it is not always possible to fit the number of dimensions corresponding to $L = 16$, especially for

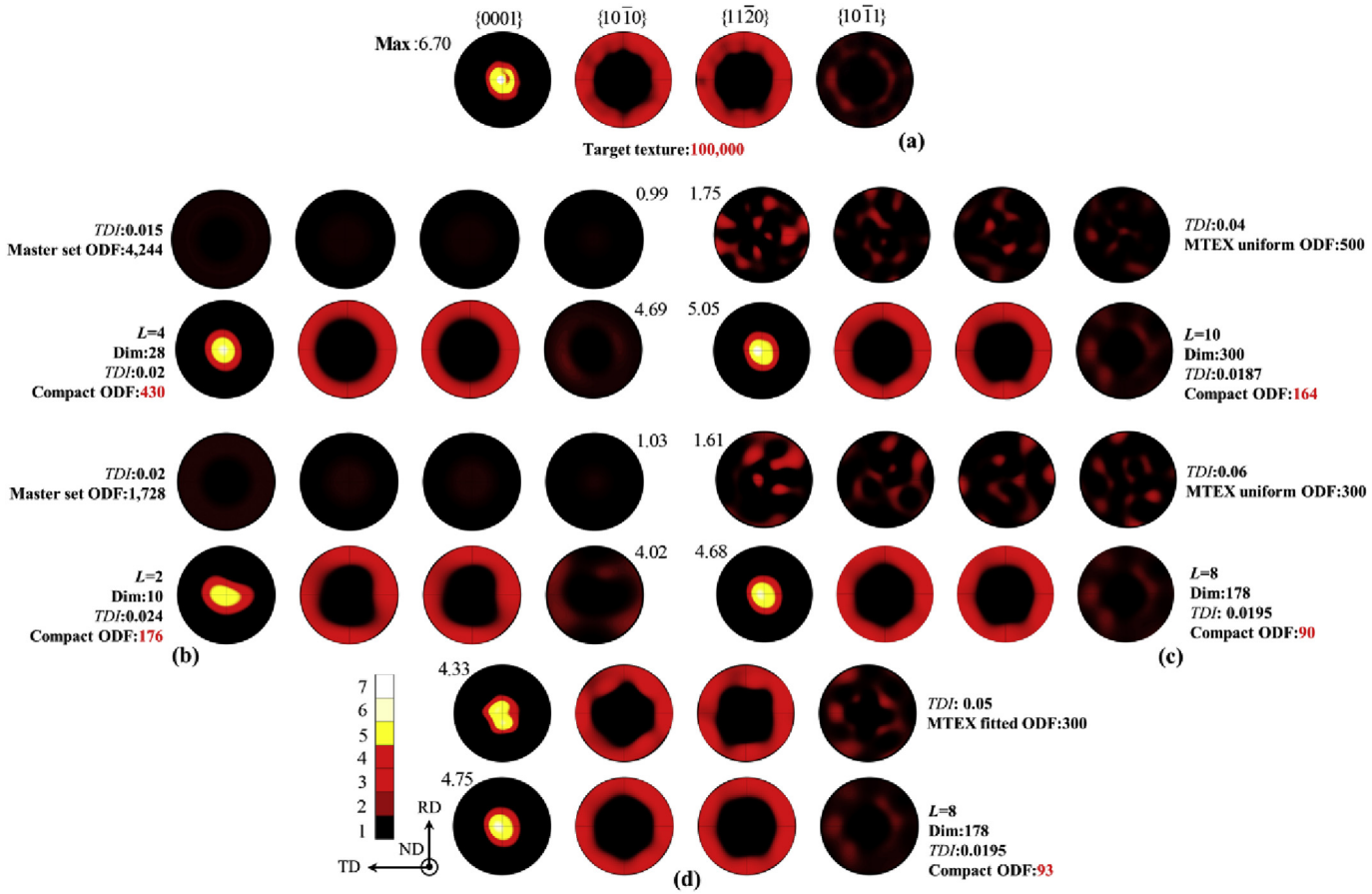

Fig. 5. Compact reconstruction of HCP-triclinic target ODF of CR pure α-Zr. Details in the figure are the same as those in Fig. 4 (see the caption of Fig. 4).

low symmetry structures. The *TDI* is calculated using

$$TDI = \frac{\sqrt{\int_{FZ}\left(f(g)-\widehat{f}(g)\right)^2 dg}}{\sqrt{\int_{FZ}\left(f(g)-\tilde{f}(g)\right)^2 dg}} = \frac{\sqrt{\sum_l\sum_\mu\sum_\nu\left(\overline{F}_l^{\mu\nu}-\widehat{F}_l^{\mu\nu}\right)^2}}{\sqrt{\sum_l\sum_\mu\sum_\nu\left(\overline{F}_l^{\mu\nu}-\tilde{F}_l^{\mu\nu}\right)^2}} \quad (17)$$

where, $\overline{F}_l^{\mu\nu}$ and $\widehat{F}_l^{\mu\nu}$ denote the expansion coefficients for the target ODF ($f(g)$) and compact ODF ($\widehat{f}(g)$), respectively. The right hand side of Eq. (17) is readily obtained taking the advantage of the rule for real functions that $f(g) = F_l^{\mu\nu}\dddot{T}_l^{\mu\nu}(g) = F_l^{*\mu\nu}\dddot{T}_l^{*\mu\nu}(g)$. The normalization term represents the distance from the target to the furthest point in the respected convex hull made up of the expansion coefficients corresponding to a uniform ODF ($\tilde{f}(g)$). Here, the superscript ($\sim$) is used to indicate a uniform (or a random) ODF. The *TDI* value of zero indicates identical ODFs, while a value of unity indicates maximum theoretical disagreement between two ODFs. Note also that the following hold true for the normalized ODFs $\int_{FZ} f(g)dg = \int_{FZ}\widehat{f}(g)dg = \int_{FZ}\tilde{f}(g)dg = 1$. Note that *TDI* values are always calculated for $L = 16$. Thus, if the fit between a target and a compact representation achieved the accuracy of $L = 16$, then $TDI \approx 0$ and the solution is regarded as the exact. However, if the fit achieved $L < 16$ then $TDI > 0$. The *TDI* value is influenced by the 'trailing' expansion coefficients that were not fit. These coefficients are set to zero for the *TDI* calculations. Additionally, the *TDI* value can change with choosing another normalization term such as the largest distance in the respected hull.

The procedure is applied to several material systems, and the results are presented and discussed in the next section.

4. Results

Table 4 presents material systems used in the study. The systems are chosen to cover a broad range of crystal and sample symmetries as well as to show that the developed procedure is independent on techniques used to determine the measured full-size ODFs. The techniques for measuring ODF are broadly classified according to whether they measure macro-texture or micro-texture. The former includes X-ray diffraction (XRD) and neutron diffraction while the latter is based on electron backscattered diffraction (EBSD). While the ODF is directly available from an EBSD measurement, it needs to be calculated based on the pole figures for XRD and Neutron measurements. The number of crystal orientations in the calculated ODF is appropriately chosen to capture the pole figure measurements.

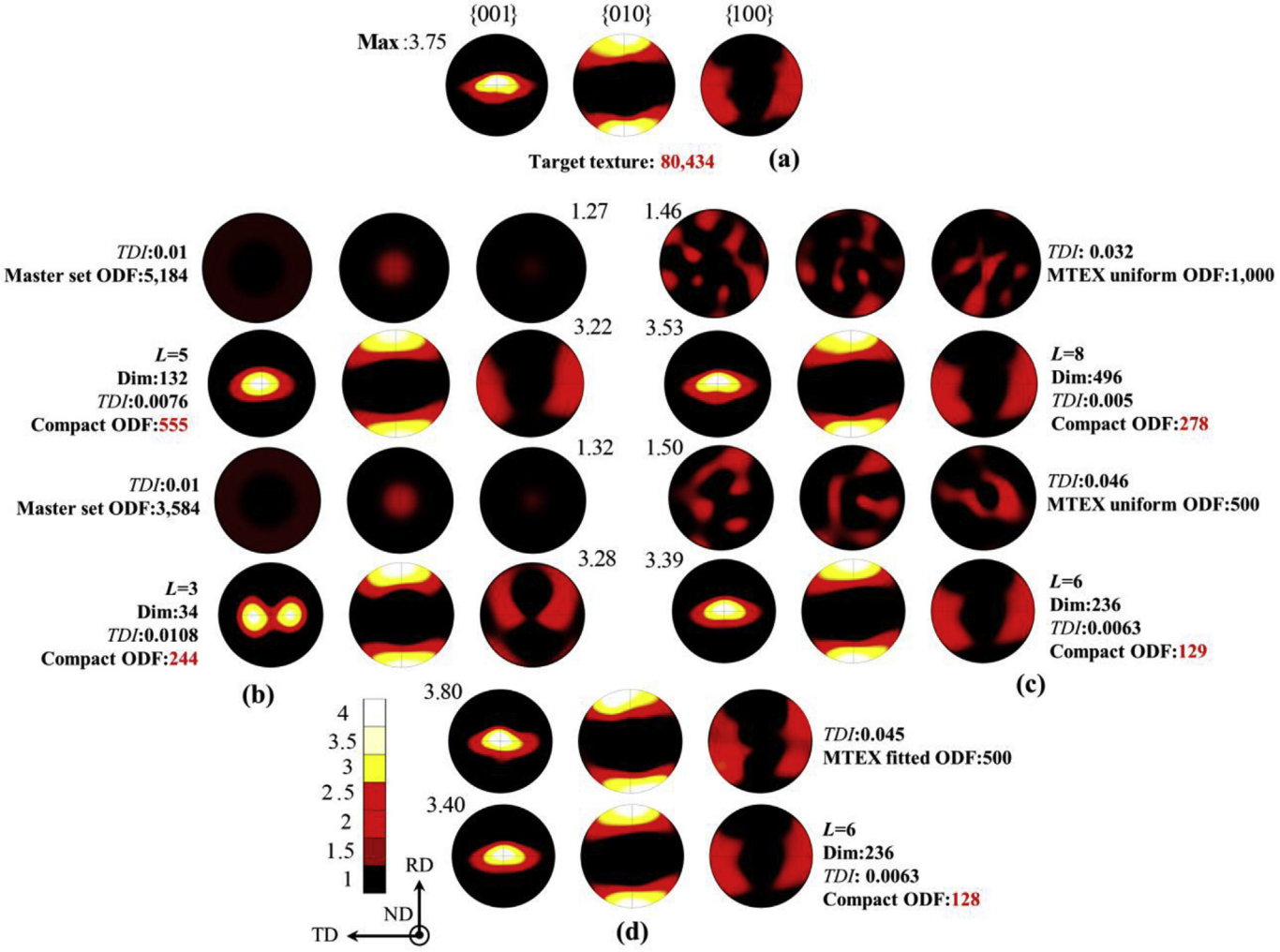

Fig. 6. Compact reconstruction of orthorhombic-triclinic target ODF of SR α-U. Details in the figure are the same as those in Fig. 4 (see the caption of Fig. 4).

The alloy AA6022-T4 [16,75] was a rolled sheet having an approximately orthotropic texture, which was measured using EBSD. This texture is further made orthotropic by artificially enforcing the sample symmetry. Pure Ta was also a rolled sheet whose texture was measured by XRD and was found orthotropic looking as well [76]. While the alloy AA6022-T4 is an example of face-centered cubic (FCC) material, pure Ta is a body-centered cubic (BCC) material. An example of a cubic-triclinic texture is created numerically by performing a simple shear simulation of an initially uniform texture of pure Cu using a crystal plasticity model. Examples of hexagonal materials include a clock rolled (CR) pure α-Zr [77], a straight rolled (SR) rare earth Mg alloy WE43 [78–81], and SR high-purity α-Ti [30]. Geometries of crystal lattices in these materials differ in their c/a ratio. Moreover, they have been measured using three different techniques. Finally, α-U is considered as the material with the lowest level of crystal symmetry, which is orthotropic. The material was processes in three different ways CR, SR and swaged (SW) resulting in three different ODFs, which were measured by EBSD over large areas [82]. Table 4 presents the number of crystal orientations for every measured ODF.

The compact reconstruction of the above target ODFs is performed using the developed procedure. Figs. 4–6 present the results for AA6022-T4, pure α-Zr, and depleted α-U (SR), respectively in terms of stereographic pole figures plotted in the TSL software [70]. More results are provided in the supplementary material of the paper (Figs. A1-A6). The target ODFs are always plotted with $L = 16$. Three compact ODFs were used in every case. Furthermore, two master set ODFs and two MTEX uniform ODFs are considered. The effort was made to obtain compact ODFs for $L = 16$. *TDI* was used to quantify the quality of the fits. For the high symmetry cases like FCC and BCC, the linprog solver was capable of fitting all dimensions (denoted by 'Dim' in the figures) corresponding to $L = 16$. Therefore, *TDI* shows almost perfect match. However, for some cases we accepted fits corresponding to $L < 16$, especially for the low symmetry structures. Note that the TSL software requires entering L for plotting pole figures from either ODF or its representation. Therefore, we performed the reconstruction for given L values, although it was possible to fit more dimensions but less than the next L value. In these cases, L used to plot pole figures corresponded to that of fits. *TDI* for these cases was essentially the difference between the fitted ODF to a given L value and the corresponding target ODF for $L = 16$. We point out that fitting higher number of dimensions ($L = 16$) was always possible but with larger number of orientations in the compact ODFs. Thus, there is a tradeoff between the quality of fit and size of the compact ODF. Figs. 4–6 and A1–A6 demonstrate this tradeoff.

We find that the use of MTEX uniform and MTEX fitted compact ODFs are more flexible in terms of the number of orientations per

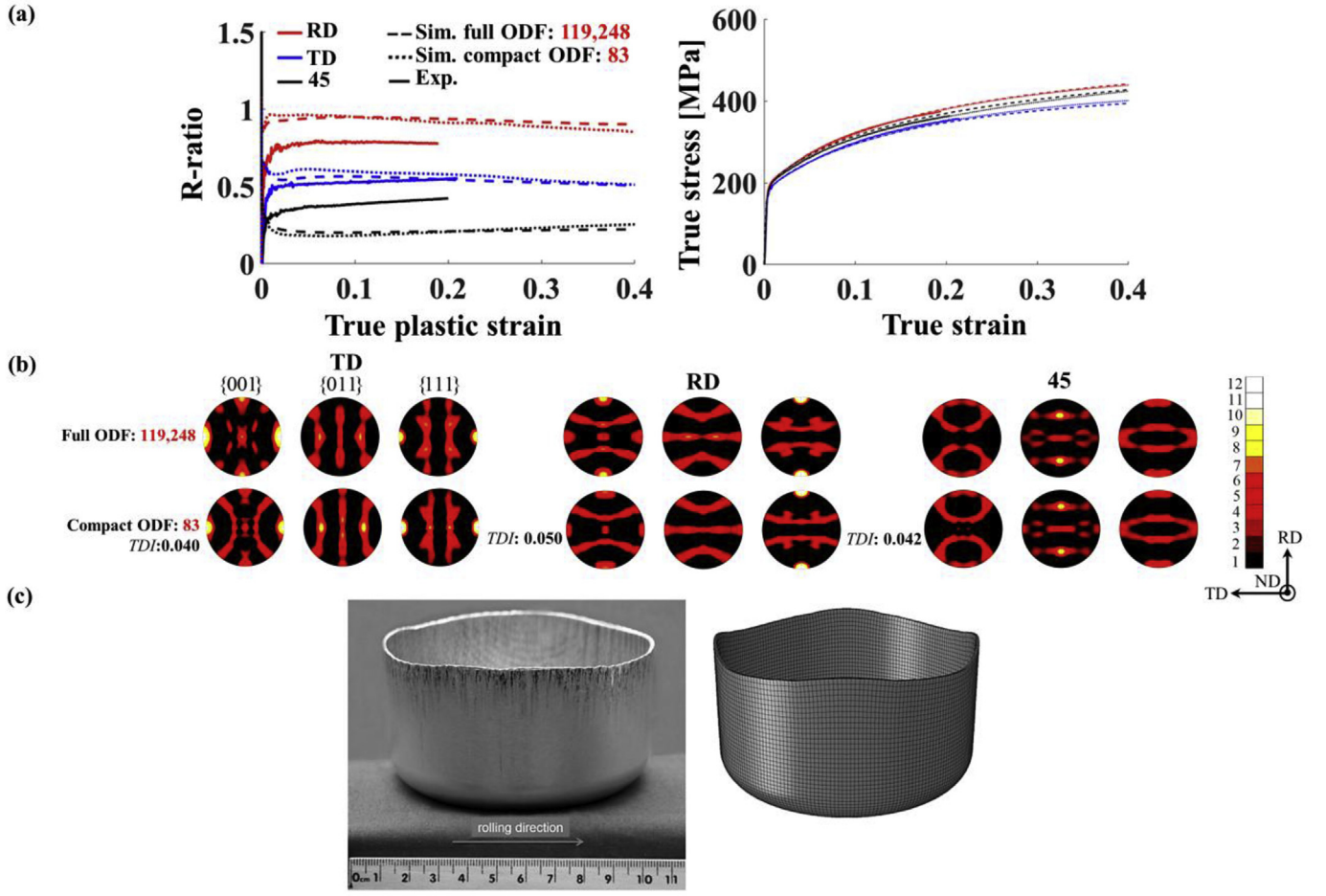

Fig. 7. (a) Comparison of measured and simulated by EPSC quasi-static true stress–true strain responses in tension and R-ratio along the three loading directions as indicated in the legend for AA6022-T4. Simulations were performed using the full ODF and the compact ODF as indicated in the legend. (b) Pole figures showing predicted texture evolution after simple tension at a true strain of 0.6. (c) Photograph of a drawn-cup from AA6022-T4 sheet and predicted geometry using FE-EPSC showing the formation of four ears. Also indicated is the rolling direction (RD = x, TD = z). ¼ of the blank consisted of 14,560 C3D8R elements was simulated. The FE-EPSC simulation was performed using the compact ODF embedded at each FE integration point.

compact ODF and yields better results compared to the rigid master set ODFs. The MTEX compact ODFs allowed us to use higher L values and, as a result, more dimensions were fit. More terms in the expansion results in more detailed reconstruction. For example, for the α-Ti case or SW α-U uranium, the use of mater set ODFs forced us to choose very low L values to fit the target using a reasonable number of grains (i.e. not more than 300 grains). Compact ODFs generated using MTEX allowed us to use high values for L and consequently improve the quality of fits. Moreover, a closer initial guess provided by MTEX fitted ODF significantly helps the iterative fitting procedure so the linear programming solver converges faster.

5. Discussion

The procedure advanced in this paper is a rigorous methodology for the compaction of large crystallographic texture data. We have showed that any statistical ODF containing any number of orientations can be reconstructed with a compact ODF containing a significantly smaller but representative set of orientations. This was possible taking the advantage of the GSH representation and the linearity of the expansion space.

During plastic deformation, orientations within a polycrystalline metal reorient and as a result an initial ODF evolves. ODF evolution can be captured using crystal plasticity models such as VPSC or EPSC. These models consider the operating slip and twin systems. Questions like whether a compact ODF is sufficient to capture stress-strain response to large strains, texture evolution, evolution of twin volume fractions, and ultimately geometrical changes of the samples could arise.

We now present several case studies of different complexity to fully validation of the procedure in every aspect mentioned above. Fig. 7 compares the measured and simulated quasi-static true stress–true strain responses in tension and R-ratio along the three loading directions for AA6022-T4. The simulations were performed using the full ODF and the compact ODF consisting of only 83 weighted crystal orientations using EPSC. Pole figures show the texture evolution in tension to a strain of 0.6 is predicted well with the compact ODF. Details of the material model can be found in Ref. [16]. The comparison of a drawn-cup photograph and predicted geometry using FE-EPSC shows that the model captures the formation of four ears. More details about the cup drawing experimental setup can be found in Ref. [83]. Details for the FE-EPSC formulation can be found in Refs. [26,38,84]. ¼ of the blank

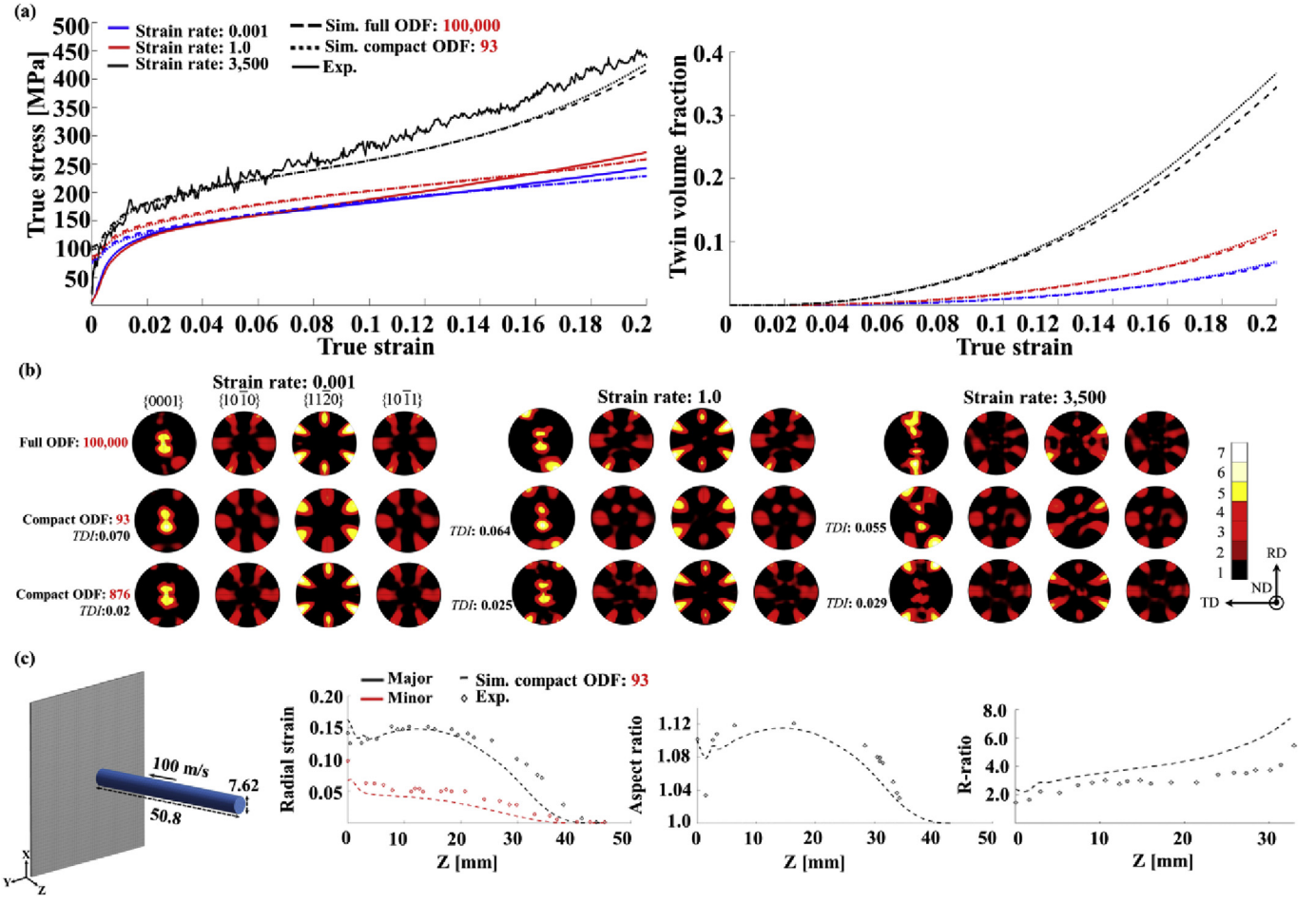

Fig. 8. (a) Comparison of measured and simulated by VPSC true stress–true strain responses in compression along the in-plane (RD) direction of CR α-Zr under strain rates as indicated in the legend. Evolution of twin volume fraction predicted by the model is also presented. Simulations were performed using the full ODF and the compact ODF as indicated in the legend. (b) Pole figures showing predicted texture evolution after in-plane compression at a true strain of 0.2. (c) FE model for simulating the Zr Taylor impact test using FE-VPSC. ¼ of the cylinder consisted of 405 C3D8 elements was simulated. Comparison of measured and predicted geometrical changes: major and minor radial strain plot showing the elliptical cross-sectional shape formed from the foot to about 40 mm from the foot, aspect ratio plot depicting the ratio between the major and minor axis of the cylinder, and R-value plot showing the ratio between the major radial strain and the minor radial strain. The FE-VPSC simulation was performed using the compact ODF: 93 embedded at each FE integration point.

consisted of 14,560 C3D8R elements was simulated. The FE-EPSC simulation was performed using the compact ODF embedded at each FE integration point.

While the FCC metals deform with one slip mode, the HCP and orthorhombic metals deforms by multiple slip and twinning modes. The next two case studies are for these low symmetry metals. Fig. 8 compares measured and simulated true stress–true strain responses in compression along the in-plane direction for

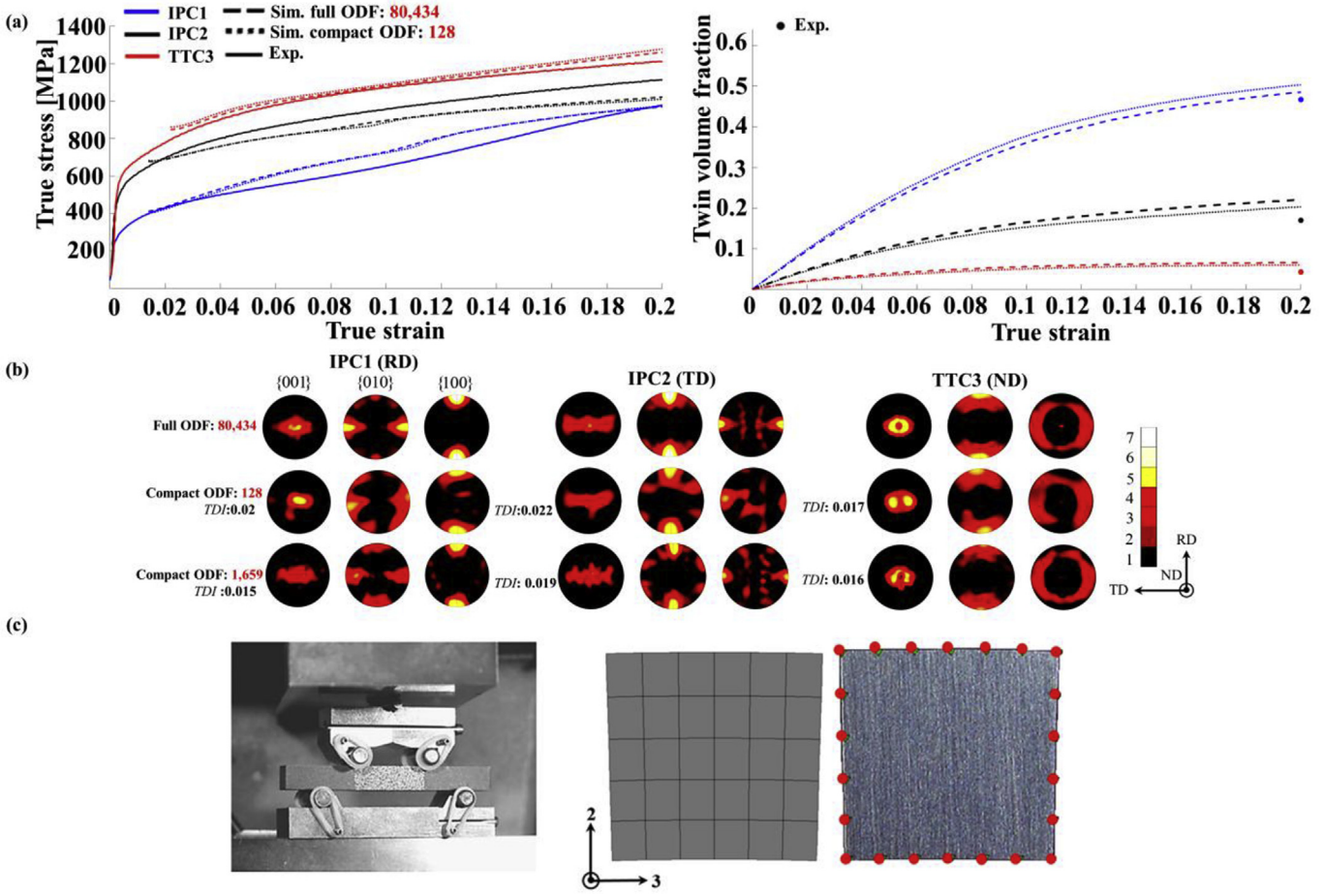

Fig. 9. (a) Comparison of measured and simulated by VPSC quasi-static true stress–true strain responses in compression along the three directions for SR α-U. Evolution of twin volume fraction predicted by the model is also presented. Simulations were performed using the full ODF and the compact ODF as indicated in the legend. (b) Pole figures showing predicted texture evolution after compression at a true strain of 0.2. (c) Comparison of the predicted and measured beam cross-section for the beam of SR α-U. The external nodal coordinates of the deformed FE model are superimposed on the photographed experimentally deformed beam. ¼ of the beam consisted of 300 C3D20R elements was simulated. The FE-VPSC simulation was performed using the compact ODF: 128 embedded at each FE integration point.

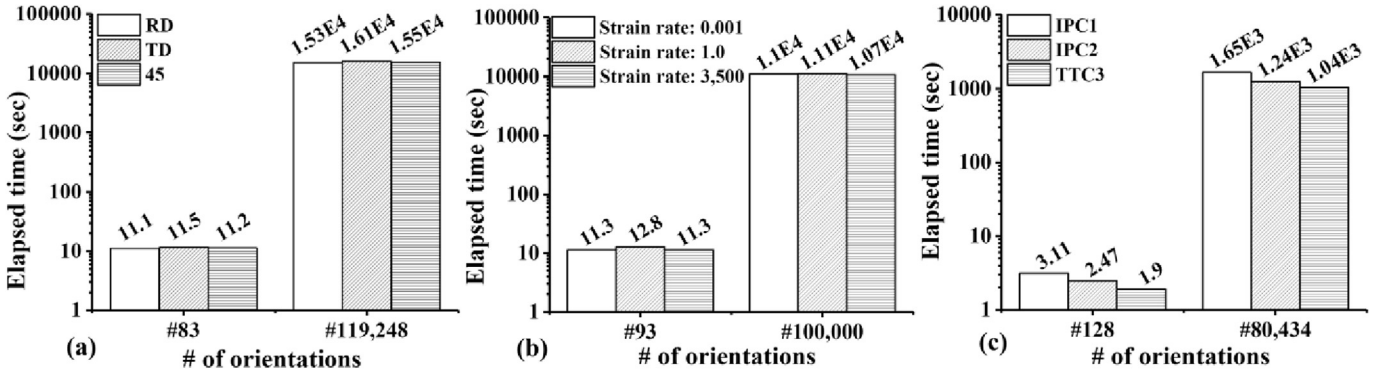

Fig. 10. Comparison of the computational time involved in the standalone model simulations using the compact ODF and the full ODF for: (a) AA6022-T4, (b) Pure α-Zr, and (c) SR α-U. The rate sensitivity exponent of the visco-plastic power law known to influence the number of iterations and computational time of VPSC was set to 50. The simulations were run to a total strain of 0.2 in 200 strain increments for VPSC and 1500 strain increments for EPSC, which is an explicit code demanding more increments to ensure the accuracy. Note that the α-Zr simulations are longer than the α-U simulations because of modeling of both primary and secondary twinning reorientation in α-Zr, while only primary twinning was modeled in α-U. All simulation were run on a single core of Intel(R) Xeon(R) CPU E5-2699 v4 @ 2.20 GHz.

Table 5
Comparison of the computational time involved in the FEM simulations using the compact ODFs and the full ODFs.

Simulation type	# of orientations (compact/full)	Elapsed time (days)	# of processors	Processor type
AA6022-T4 cup drawing	83/119,248	2.92/4051.8	30	Intel(R) Xeon(R) CPU E5-2695 v4 @ 2.10 GHz
Pure α-Zr Taylor impact	93/100,000	1.1/1019.2	34	
Depleted α-U (SR) beam bending	128/80,434	0.33/173.38	32	

CR α-Zr under several strain rates. Additionally, the evolution of twin volume fraction predicted by the model is presented. Simulations were performed using the full ODF and the compact ODF consisting of 93 crystal orientations using VPSC. Details for this model can be found in Ref. [77]. Pole figures showing predicted texture evolution after the compression at a true strain of 0.2 are also shown. Predictions using a larger compact ODF fit to $L = 16$ are also shown. Finally, geometrical changes simulated using FE-VPSC for the Zr Taylor impact test are shown [85]. ¼ of the cylinder consisted of 405 C3D8 elements was simulated like in our earlier work [85]. Comparison of measured and predicted geometrical changes in terms of the major and minor radial strain, aspect ratio, and R-value demonstrate the accuracy of the simulation. The FE-VPSC simulation was performed using the compact ODF embedded at each FE integration point.

Finally, Fig. 9 shows similar information for SR α-U. Measured and simulated quasi-static true stress–true strain responses in compression along the three directions are presented along with the evolution of twin volume fractions. As before, the simulations were performed using the full ODF and the compact ODF consisting of 128 crystal orientations using VPSC [29,86]. Pole figures showing predicted texture evolution after compression at a true strain of 0.2 are also presented. The larger compact ODF was fit to $L = 14$. Evidently, the compact ODF with more weighted crystal orientations more accurately capture texture evolution. The predicted and measured beam cross-section for the beam are compared to demonstrate accuracy of the model to capture geometrical changes. The external nodal coordinates of the deformed FE model are superimposed on the photographed experimentally deformed beam taken from Ref. [24]. ¼ of the beam consisted of 300 C3D20R elements was simulated. The FE-VPSC simulation was performed using the compact ODF embedded at each FE integration point.

Fig. 10 shows the comparison of the computational time involved in the standalone simulations using the compact ODFs and the full ODFs. As expected, the scalability is approximately linear. Comparison of the computational time involved in the FEM simulations is given in Table 5. The elapsed times for the simulations using compact ODFs are recorded. However, the FEM simulations involving the full ODFs at every FE integration point are computationally challenging for a regular computer workstation. The values shown for the full ODFs are estimates based on the scalabilities of the standalone simulations and the FEM simulations involving the compact ODFs at every FE integration point. Clearly, the simulations with experimentally measured textures are impractical.

The case studies show that the compact ODFs capture every aspect of deformation behavior with great accuracy. Thus, a dramatic data compaction is possible using the GSH functions without losing accuracy in the predictions. The computing time involved in polycrystal plasticity models increases almost linearly with the number of crystal orientations considered in simulations. Thus, the speedups are directly proportional to the compaction of crystal orientations. These speedups are critically needed for enabling large scale crystal plasticity finite element simulations. The procedure developed in the present paper is primarily intended to increase efficiency of these codes.

The methods for determining the compact set ODFs used in the present work can be regarded as brute force methods. Future research will focus on establishing a more sophisticated procedure to find the minimal set of crystallographic orientations for the compact ODF for every crystal and sample symmetry. To this end, orientations corresponding to the boundary points of the compact and convex texture hulls in multiple dimensions (Fig. 3) would be sought. As explained earlier, the convex hull for a given crystal and sample contains all physically realizable textures, and theoretically, the compact set of orientations that will provide the most efficient texture reconstruction is one that is comprised of crystal orientations with expansion coefficients that form the boundary for this convex region up to the desired number of dimensions. The main challenge encountered in attempting this concept is finding the vertices of the texture hull in fairly large dimensional spaces. Alternatively, orientations corresponding to minimum and maximum value for each expansion coefficient for each non-zero frequency (Table 3) could be selected and further prioritized to maximize the compaction.

The developed procedure is restricted to finding compact ODFs. Future work will also attempt to further generalize the procedure to finding statistically representative volume elements, which would consider not only ODF information but also spatially resolved explicit microstructural features [87,88]. The present work formed solid bases for such future developments.

6. Conclusions

Metal forming process simulations using ODF sensitive crystal plasticity models are impractical in part because of the need to store many state variables including the ODF data. The computational time involved in such calculations scales linearly with the number of crystal orientations. This work successfully advanced the procedure for the compaction of the ODF data of any size to computationally manageable compact ODFs. The extended procedure can consider low symmetry crystal structures and triclinic sample symmetry. The procedure is based on the spectral representation of ODFs using the GSH functions. The core procedure consists of matching the spectral representation of a full-size ODF containing any number of crystal orientations with that of an ODF containing a compact set of orientations. The procedure is fully automated using an algorithm developed in MATLAB. Case studies of ODF compaction showed that the procedure can accurately compact large data ODFs to significantly smaller sets of weighted orientations on the order of approximately 100. The procedure was applied to metals with cubic, hexagonal, and orthorhombic crystal structures with orthotropic and triclinic sample symmetries and shown to work well for all these metals, some of which deform by both slip and twinning. It is quantitatively demonstrated that texture evolution, twin volume fraction evolution, stress-strain response, and geometrical changes of samples can be accurately simulated to large plastic strains with compact ODFs using crystal plasticity finite element models with dramatic reduction in computational time involved.

Acknowledgments

This work is based upon a project supported by the U.S. National Science Foundation under CAREER grant no. CMMI-1650641.

Appendix A. Supplementary data

Supplementary data related to this article can be found at https://doi.org/10.1016/j.actamat.2018.06.017.

References

[1] H.-J. Bunge, Texture analysis in materials science, in: Mathematical Methods, Cuvillier Verlag, Göttingen, 1993.
[2] B.L. Adams, T. Olson, Mesostructure - properties linkage in polycrystals, Prog. Mater. Sci. 43 (1998) 1–88.
[3] U.F. Kocks, C.N. Tomé, H.-R. Wenk, Texture and Anisotropy, Cambridge University Press, Cambridge, UK, 1998.
[4] L.E. Fuentes-Cobas, A. Muñoz-Romero, M.E. Montero-Cabrera, L. Fuentes-Montero, M.E. Fuentes-Montero, Predicting the coupling properties of axially-textured materials, Materials 6 (2013) 4967–4984.
[5] B.S. Fromm, B.L. Adams, S. Ahmadi, M. Knezevic, Grain size and orientation distributions: application to yielding of α-titanium, Acta Mater. 57 (2009) 2339–2348.
[6] G.I. Taylor, Plastic strain in metals, J. Inst. Met. 62 (1938) 307–324.
[7] M. Knezevic, S.R. Kalidindi, D. Fullwood, Computationally efficient database and spectral interpolation for fully plastic Taylor-type crystal plasticity calculations of face-centered cubic polycrystals, Int. J. Plast. 24 (2008) 1264–1276.
[8] G. Sachs, Zur ableitung einer fliessbedingung. Mitteilungen der deutschen Materialprüfungsanstalten, Springer, 1929, pp. 94–97.
[9] M. Knezevic, S.R. Kalidindi, Fast computation of first-order elastic-plastic closures for polycrystalline cubic-orthorhombic microstructures, Comput. Mater. Sci. 39 (2007) 643–648.
[10] R.A. Lebensohn, C.N. Tomé, A self-consistent anisotropic approach for the simulation of plastic deformation and texture development of polycrystals: application to zirconium alloys, Acta Metall. Mater. 41 (1993) 2611–2624.
[11] R.A. Lebensohn, M. Zecevic, M. Knezevic, R.J. McCabe, Average intragranular misorientation trends in polycrystalline materials predicted by a viscoplastic self-consistent approach, Acta Mater. 104 (2016) 228–236.
[12] M. Jahedi, I.J. Beyerlein, M.H. Paydar, M. Knezevic, Effect of Grain Shape on Texture Formation during Severe Plastic Deformation of Pure Copper Advanced Engineering Materials, vol. 20, 2018, p. 1600829.
[13] M. Knezevic, I.J. Beyerlein, T. Nizolek, N.A. Mara, T.M. Pollock, Anomalous basal slip activity in zirconium under high-strain deformation, Mater. Res. Lett. 1 (2013) 133–140.
[14] M. Knezevic, T. Nizolek, M. Ardeljan, I.J. Beyerlein, N.A. Mara, T.M. Pollock, Texture evolution in two-phase Zr/Nb lamellar composites during accumulative roll bonding, Int. J. Plast. 57 (2014) 16–28.
[15] P.A. Turner, C.N. Tomé, A study of residual stresses in Zircaloy-2 with rod texture, Acta Metall. Mater. 42 (1994) 4143–4153.
[16] M. Zecevic, M. Knezevic, A dislocation density based elasto-plastic self-consistent model for the prediction of cyclic deformation: application to Al6022-T4, Int. J. Plast. 72 (2015) 200–217.
[17] S.R. Kalidindi, C.A. Bronkhorst, L. Anand, Crystallographic texture evolution in bulk deformation processing of FCC metals, J. Mech. Phys. Solid. 40 (1992) 537–569.
[18] M. Knezevic, B. Drach, M. Ardeljan, I.J. Beyerlein, Three dimensional predictions of grain scale plasticity and grain boundaries using crystal plasticity finite element models, Comput. Meth. Appl. Mech. Eng. 277 (2014) 239–259.
[19] M. Ardeljan, I.J. Beyerlein, M. Knezevic, A dislocation density based crystal plasticity finite element model: application to a two-phase polycrystalline HCP/BCC composites, J. Mech. Phys. Solid. 66 (2014) 16–31.
[20] M. Ardeljan, M. Knezevic, T. Nizolek, I.J. Beyerlein, N.A. Mara, T.M. Pollock, A study of microstructure-driven strain localizations in two-phase polycrystalline HCP/BCC composites using a multi-scale model, Int. J. Plast. 74 (2015) 35–57.
[21] M. Ardeljan, I.J. Beyerlein, M. Knezevic, Effect of dislocation density-twin interactions on twin growth in AZ31 as revealed by explicit crystal plasticity finite element modeling, Int. J. Plast. 99 (2017) 81–101.
[22] R.A. Lebensohn, A.K. Kanjarla, P. Eisenlohr, An elasto-viscoplastic formulation based on fast Fourier transforms for the prediction of micromechanical fields in polycrystalline materials, Int. J. Plast. 32–33 (2012) 59–69.
[23] A. Eghtesad, M. Zecevic, R.A. Lebensohn, R.J. McCabe, M. Knezevic, Spectral database constitutive representation within a spectral micromechanical solver for computationally efficient polycrystal plasticity modelling, Comput. Mech. 61 (2018) 89–104.
[24] M. Knezevic, R.J. McCabe, R.A. Lebensohn, C.N. Tomé, C. Liu, M.L. Lovato, B. Mihaila, Integration of self-consistent polycrystal plasticity with dislocation density based hardening laws within an implicit finite element framework: application to low-symmetry metals, J. Mech. Phys. Solid. 61 (2013) 2034–2046.
[25] J. Segurado, R.A. Lebensohn, J. Llorca, C.N. Tomé, Multiscale modeling of plasticity based on embedding the viscoplastic self-consistent formulation in implicit finite elements, Int. J. Plast. 28 (2012) 124–140.
[26] M. Zecevic, I.J. Beyerlein, M. Knezevic, Coupling elasto-plastic self-consistent crystal plasticity and implicit finite elements: applications to compression, cyclic tension-compression, and bending to large strains, Int. J. Plast. 93 (2017) 187–211.
[27] A.J. Beaudoin, K.K. Mathur, P.R. Dawson, G.C. Johnson, Three-dimensional deformation process simulation with explicit use of polycrystal plasticity models, Int. J. Plast. 9 (1993) 833–860.
[28] M. Knezevic, R.J. McCabe, R.A. Lebensohn, C.N. Tomé, B. Mihaila, Finite element implementation of a self-consistent polycrystal plasticity model: Application to α-uranium, in: Proceedings: Volume 2: Materials Properties, Characterization, and Modeling TMS (The Minerals, Metals & Materials Society), 2012, pp. 789–796.
[29] M. Knezevic, R.J. McCabe, C.N. Tomé, R.A. Lebensohn, S.R. Chen, C.M. Cady, G.T. Gray Iii, B. Mihaila, Modeling mechanical response and texture evolution of α-uranium as a function of strain rate and temperature using polycrystal plasticity, Int. J. Plast. 43 (2013) 70–84.
[30] M. Knezevic, R.A. Lebensohn, O. Cazacu, B. Revil-Baudard, G. Proust, S.C. Vogel, M.E. Nixon, Modeling bending of α-titanium with embedded polycrystal plasticity in implicit finite elements, Mater. Sci. Eng., A 564 (2013) 116–126.
[31] Balasubramanian, Single crystal and polycrystal elasto-viscoplasticity: application to earing in cup drawing of F.C.C. materials, Comput. Mech. 17 (1996) 209–225.
[32] D. Raabe, F. Roters, Using texture components in crystal plasticity finite element simulations, Int. J. Plast. 20 (2004) 339–361.
[33] A.J. Beaudoin, P.R. Dawson, K.K. Mathur, U.F. Kocks, D.A. Korzekwa, Application of polycrystal plasticity to sheet forming, Comput. Meth. Appl. Mech. Eng. 117 (1994) 49–70.
[34] A. Kumar, P. Dawson, Polycrystal plasticity modeling of bulk forming with finite elements over orientation space, Comput. Mech. 17 (1995) 10–25.
[35] M. Knezevic, M. Jahedi, Y.P. Korkolis, I.J. Beyerlein, Material-based design of the extrusion of bimetallic tubes, Comput. Mater. Sci. 95 (2014) 63–73.
[36] M. Zecevic, R.J. McCabe, M. Knezevic, Spectral database solutions to elasto-viscoplasticity within finite elements: application to a cobalt-based FCC superalloy, Int. J. Plast. 70 (2015) 151–165.
[37] M. Jahedi, M. Knezevic, M. Paydar, High-Pressure double torsion as a severe plastic deformation process: experimental procedure and finite element modeling, J. Mater. Eng. Perform. 24 (2015) 1471–1482.
[38] M. Zecevic, M. Knezevic, Modeling of sheet metal forming based on implicit embedding of the elasto-plastic self-consistent formulation in shell elements: application to cup drawing of AA6022-T4, JOM (J. Occup. Med.) 69 (2017) 922–929.
[39] N. Barton, J. Bernier, J. Knap, A. Sunwoo, E. Cerreta, T. Turner, A call to arms for task parallelism in multi-scale materials modeling, Int. J. Numer. Meth. Eng. 86 (2011) 744–764.
[40] N.R. Barton, J. Knap, A. Arsenlis, R. Becker, R.D. Hornung, D.R. Jefferson, Embedded polycrystal plasticity and adaptive sampling, Int. J. Plast. 24 (2008) 242–266.
[41] S.R. Kalidindi, H.K. Duvvuru, M. Knezevic, Spectral calibration of crystal plasticity models, Acta Mater. 54 (2006) 1795–1804.
[42] J.B. Shaffer, M. Knezevic, S.R. Kalidindi, Building texture evolution networks for deformation processing of polycrystalline fcc metals using spectral approaches: applications to process design for targeted performance, Int. J. Plast. 26 (2010) 1183–1194.
[43] M. Knezevic, S.R. Kalidindi, R.K. Mishra, Delineation of first-order closures for plastic properties requiring explicit consideration of strain hardening and crystallographic texture evolution, Int. J. Plast. 24 (2008) 327–342.
[44] X. Wu, G. Proust, M. Knezevic, S.R. Kalidindi, Elastic-plastic property closures for hexagonal close-packed polycrystalline metals using first-order bounding theories, Acta Mater. 55 (2007) 2729–2737.
[45] H.K. Duvvuru, M. Knezevic, R.K. Mishra, S.R. Kalidindi, Application of microstructure sensitive design to FCC polycrystals, Mater. Sci. Forum 546 (2007) 675–680.
[46] M. Knezevic, H.F. Al-Harbi, S.R. Kalidindi, Crystal plasticity simulations using discrete Fourier transforms, Acta Mater. 57 (2009) 1777–1784.
[47] H.F. Al-Harbi, M. Knezevic, S.R. Kalidindi, Spectral approaches for the fast computation of yield surfaces and first-order plastic property closures for polycrystalline materials with cubic-triclinic textures, CMC: Computers, Materials, & Continua 15 (2010) 153–172.
[48] M. Zecevic, R.J. McCabe, M. Knezevic, A new implementation of the spectral crystal plasticity framework in implicit finite elements, Mech. Mater. 84 (2015) 114–126.
[49] N. Landry, M. Knezevic, Delineation of first-order elastic property closures for hexagonal metals using fast fourier transforms, Materials 8 (2015) 6326–6345.
[50] V. Sundararaghavan, N. Zabaras, Linear analysis of texture-property relationships using process-based representations of Rodrigues space, Acta Mater. 55 (2007) 1573–1587.
[51] B. Mihaila, M. Knezevic, A. Cardenas, Three orders of magnitude improved efficiency with high-performance spectral crystal plasticity on GPU platforms, Int. J. Numer. Meth. Eng. 97 (2014) 785–798.
[52] M. Knezevic, D.J. Savage, A high-performance computational framework for fast crystal plasticity simulations, Comput. Mater. Sci. 83 (2014) 101–106.
[53] A. Eghtesad, K. Germaschewski, I.J. Beyerlein, A. Hunter, M. Knezevic, Graphics processing unit accelerated phase field dislocation dynamics: application to bi-metallic interfaces, Adv. Eng. Software 115 (2018) 248–267.
[54] D.J. Savage, M. Knezevic, Computer implementations of iterative and non-iterative crystal plasticity solvers on high performance graphics hardware, Comput. Mech. 56 (2015) 677–690.

[55] S.I. Wright, B.L. Adams, An evaluation of the single orientation method for texture determination in materials of moderate texture strength, Textures Microstruct. 12 (1990) 65–76.
[56] J. Pospiech, J. Jura, G. Gottstein, Statistical analysis of single grain orientation data generated from model textures, in: Material Science Forum, 157, Trans Tech Publ, 1994, pp. 407–412.
[57] T. Baudin, R. Penelle, Determination of the total texture, MTA 24 (1993) 2299–2311.
[58] T. Baudin, J. Jura, R. Penelle, J. Pospiech, Estimation of the minimum grain number for the orientation distribution function calculation from individual orientation measurements on Fe-3% Si and Ti-4Al-6V alloys, J. Appl. Crystallogr. 28 (1995) 582–589.
[59] M. Knezevic, N.W. Landry, Procedures for reducing large datasets of crystal orientations using generalized spherical harmonics, Mech. Mater. 88 (2015) 73–86.
[60] S.R. Kalidindi, M. Knezevic, S. Niezgoda, J. Shaffer, Representation of the orientation distribution function and computation of first-order elastic properties closures using discrete Fourier transforms, Acta Mater. 57 (2009) 3916–3923.
[61] F.C. Frank, Orientation Mapping, MTA 19A, 1987, pp. 403–408.
[62] P. Neumann, Representation of orientations of symmetrical objects by Rodrigues vectors, Textures Microstruct. 14-18 (1991) 53–58.
[63] Y. Takahashi, K.I. Miyazawa, M. Mori, Y. Ishida, Quaternion representation of the orientation relationship and its application to grain boundary problems, Trans. Jpn. Inst. Met 27 (1985) 345–352.
[64] I.M. Gelfand, R.A. Minlos, Z.S. Sapiro, Representations of the Rotation and Lorentz Groups and Their Applications, Pergamon Press, Oxford, London, UK, 1963.
[65] I. MathWorks, MATLAB: the Language of Technical Computing. Desktop Tools and Development Environment, Version 7, MathWorks, 2005.
[66] B.L. Adams, S. Kalidindi, D.T. Fullwood, Microstructure-sensitive Design for Performance Optimization, Butterworth-Heinemann, Waltham, MA, USA, 2013.
[67] F. Bachmann, R. Hielscher, H. Schaeben, Texture analysis with MTEX–free and open source software toolbox, Solid State Phenom. 160 (2010) 63–68.
[68] M. Lyon, B.L. Adams, Gradient-based non-linear microstructure design, J. Mech. Phys. Solid. 52 (2004) 2569–2586.
[69] S.R. Kalidindi, J.R. Houskamp, M. Lyons, B.L. Adams, Microstructure sensitive design of an orthotropic plate subjected to tensile load, Int. J. Plast. 20 (2004) 1561–1575.
[70] EDAX, TSL. Manual for Orientation Imaging Microscopy (OIM™), Version 7.1.0.
[71] T. Fast, M. Knezevic, S.R. Kalidindi, Application of microstructure sensitive design to structural components produced from hexagonal polycrystalline metals, Comput. Mater. Sci. 43 (2008) 374–383.
[72] B.L. Adams, A. Henrie, B. Henrie, M. Lyon, S.R. Kalidindi, H. Garmestani, Microstructure-sensitive design of a compliant beam, J. Mech. Phys. Solid. 49 (2001) 1639–1663.
[73] Matlab Version R2012a, The MathWorks Inc., Natick, MA, USA, 2013.
[74] M. Knezevic, A. Bhattacharyya, Characterization of microstructure in Nb rods processed by rolling: effect of grooved rolling die geometry on texture uniformity, Int. J. Refract. Metals Hard Mater. 66 (2017) 44–51.
[75] M. Zecevic, T. Roemer, M. Knezevic, Y. Korkolis, B. Kinsey, Residual ductility and microstructural evolution in continuous-bending-under-tension of AA-6022-T4, Materials 9 (2016) 130.
[76] M. Zecevic, M. Knezevic, A new visco-plastic self-consistent formulation implicit in dislocation-based hardening within implicit finite elements: application to high strain rate and impact deformation of tantalum, Comput. Meth. Appl. Mech. Eng. (2018).
[77] M. Knezevic, M. Zecevic, I.J. Beyerlein, J.F. Bingert, R.J. McCabe, Strain rate and temperature effects on the selection of primary and secondary slip and twinning systems in HCP Zr, Acta Mater. 88 (2015) 55–73.
[78] M. Jahedi, B.A. McWilliams, P. Moy, M. Knezevic, Deformation twinning in rolled WE43-T5 rare earth magnesium alloy: influence on strain hardening and texture evolution, Acta Mater. 131 (2017) 221–232.
[79] M. Jahedi, B.A. McWilliams, M. Knezevic, Deformation and fracture mechanisms in WE43 magnesium-rare earth alloy fabricated by direct-chill casting and rolling, Mater. Sci. Eng., A 726 (2018) 194–207.
[80] M. Jahedi, B.A. McWilliams, F.R. Kellogg, I.J. Beyerlein, M. Knezevic, Rate and temperature dependent deformation behavior of as-cast WE43 magnesium-rare earth alloy manufactured by direct-chill casting, Mater. Sci. Eng., A 712 (2018) 50–64.
[81] M. Jahedi, M.H. Paydar, S. Zheng, I.J. Beyerlein, M. Knezevic, Texture evolution and enhanced grain refinement under high-pressure-double-torsion, Mater. Sci. Eng., A 611 (2014) 29–36.
[82] M. Knezevic, L. Capolungo, C.N. Tomé, R.A. Lebensohn, D.J. Alexander, B. Mihaila, R.J. McCabe, Anisotropic stress-strain response and microstructure evolution of textured α-uranium, Acta Mater. 60 (2012) 702–715.
[83] H. Tian, B. Brownell, M. Baral, Y.P. Korkolis, Earing in cup-drawing of anisotropic Al-6022-T4 sheets, Int. J. Material Form. 10 (2017) 329–343.
[84] M. Zecevic, M. Knezevic, Latent hardening within the elasto-plastic self-consistent polycrystal homogenization to enable the prediction of anisotropy of AA6022-T4 sheets, Int. J. Plast. 105 (2018) 141–163.
[85] M. Zecevic, I.J. Beyerlein, R.J. McCabe, B.A. McWilliams, M. Knezevic, Transitioning rate sensitivities across multiple length scales: microstructure-property relationships in the Taylor cylinder impact test on zirconium, Int. J. Plast. 84 (2016) 138–159.
[86] M. Knezevic, J. Crapps, I.J. Beyerlein, D.R. Coughlin, K.D. Clarke, R.J. McCabe, Anisotropic modeling of structural components using embedded crystal plasticity constructive laws within finite elements, Int. J. Mech. Sci. 105 (2016) 227–238.
[87] M. Jahedi, E. Ardjmand, M. Knezevic, Microstructure metrics for quantitative assessment of particle size and dispersion: application to metal-matrix composites, Powder Technol. 311 (2017) 226–238.
[88] M. Jahedi, M.H. Paydar, M. Knezevic, Enhanced microstructural homogeneity in metal-matrix composites developed under high-pressure-double-torsion, Mater. Char. 104 (2015) 92–100.